Apparent slip and drag reduction for the flow over superhydrophobic and lubricant-impregnated surfaces

Edoardo Alinovi and Alessandro Bottaro
DICCA, Scuola Politecnica University of Genoa, 1 via Montallegro, 16145 Genoa, Italy

(Received 19 February 2018; published 13 December 2018)

The motion of a liquid above textured surfaces, impregnated with either a gas or a lubricant oil, is considered by homogenizing the microscopic near-wall flow to obtain protrusion heights (or Navier slip lengths), which can then be used in (macroscopic) direct numerical simulations of turbulence. The microstructure of the wall consists in longitudinally aligned ridges; this renders the small-scale Stokes problem amenable to decoupling into two problems, solved by the boundary element method with full account of the deformation of the liquid-lubricant interface, finally yielding two different protrusion heights, a longitudinal and a transverse one, respectively $h_{||}$ and $h_{\perp}$. Such heights are then employed in direct numerical simulations of the turbulent flow in a channel bounded by superhydrophobic or lubricant-impregnated walls, demonstrating the reduction in skin-friction drag which can be achieved with the rise in protrusion height difference, $\Delta h = h_{||} - h_{\perp}$. The results are in good agreement with an analytical approximation, provided Δh^+ (Δh scaled in wall units) remains below 2 and the protrusion heights small in magnitude.

DOI: 10.1103/PhysRevFluids.3.124002

I. INTRODUCTION

The problem of macroscopic slippage generated by microtextured surfaces has received much attention in the last few decades. The applicability of microengineered surfaces for skin-friction drag reduction is known since the seminal studies on riblets, perhaps inspired by the properties of the skin of sharks [1]. A step forward in the design of low-friction surfaces has been made by coupling the small-scale roughness elements composing the surfaces with a gas in order to create gaseous micropockets, over which a working liquid can flow with low friction. This is the case of the superhydrophobic surfaces (SHSs), which today are receiving tremendous attention. The research on SHSs has been inspired by the remarkable slipping properties of the lotus leaf [2], and many studies have been undertaken in the last few years because the potentialities of SHSs are of much interest in the field of modern microfluidics, towards the development of laboratory-on-a-chip devices for biochemical and medical purposes [3]. Also, large-scale engineering devices would take advantage of low-friction surfaces, and the maritime industry in particular could enhance the efficiency and lower emissions by using superhydrophobic coatings on the hull of ships. On the experimental side, Ou *et al.* [4] and Ou and Rothstein [5] were the first to demonstrate the drag reduction capabilities of SHSs. They focused attention on microchannels with different heights, patterned by silicon microposts or microridges at a wall, reporting a drag reduction of up to 40% in laminar conditions. Similar drag reduction was found by Choi and Kim [6] using a nanograted texture. Appreciable drag reduction in turbulent flows was observed by Ou and Rothstein [7], who studied a rectangular channel with the walls coated by polydimethylsiloxane microridges of varying span and spacing. The experiments performed in the range $2000 < \mathrm{Re} < 10\,000$ highlighted a skin-friction drag reduction of up to 50% associated with a very large value of the surface-averaged slip velocity at an effective wall coordinate. Other experimental studies [8–10] have focused more on

the local features of the slip occurring near the fluid interface and discuss in details the flow physics in the immediate proximity of the SH surface.

Despite their significant performances, the drawback encountered in using this technology is that the gaseous pockets lack robustness and can easily collapse under working conditions (under either hydrostatic pressure or shear), thus imposing severe limitations in practical applications, especially when large-scale problems and long operating times are concerned. One way to overcome this issue is to substitute the gas trapped within the wall texture with some lubricating oil, creating the so-called lubricant-impregnated surfaces (LISs). The mechanism underlying the LIS technology is essentially the same identified in the SHS: the relative slip between the two fluids triggers a skin-friction drag reduction. The usage of oil instead of gas increases the stability of the fluid-fluid interface [11] and, at the same time, exhibits interesting properties such as biofouling [12] and ice phobicity [13]. The main works on LISs have been published in more recent years. As already pointed out, on the one hand the lubricant layer is more stable, but, on the other, the skin-friction drag reduction capabilities deteriorate if the oil viscosity is large compared with the viscosity of the working fluid. This behavior was recently observed by Solomon *et al.* [14], who conducted experiments with a cone and plate rheometer. They achieved a drag reduction of 16% when the impregnating fluid was two orders of magnitude less viscous than the working fluid, but little to no drag reduction when the oil-to-fluid viscosity ratio was larger than 30. Analogous conclusions and similar drag reductions, but for a turbulent flow in a Taylor-Couette configuration at $6000 < \mathrm{Re} < 9000$, have been drawn by Rosenberg *et al.* [15]; when the viscosity ratio exceeds 30 a drag increase is found.

The key parameter to quantify the slippage generated by an SHS or LIS is related to the idea of protrusion height, or slip length, defined as the distance below the surface where the velocity extrapolates to zero. Mathematically speaking, the slip length concept allows one to model slip at a rigid wall with the help of the Navier boundary condition [16]:

$$\boldsymbol{u} = \boldsymbol{h}\left(\frac{\partial \boldsymbol{u}}{\partial y}\right), \quad \boldsymbol{h} = \mathrm{diag}(h_{||}, h_{\perp}), \tag{1}$$

where y is the wall-normal coordinate, $\boldsymbol{u}$ is the vector of velocity field components in the in-plane directions (i.e., along x and z), and $\boldsymbol{h}$ is the slip tensor, which depends on the wall texture and the properties of the lubricant fluid within the microtextured surface; the condition for the wall normal velocity is simply $v = 0$. Condition (1) gives a relation between the slip velocity and the wall shear stress and represents the most common way to model the experimental evidence of slippage over SHSs and LISs.

The first attempt to derive the slip length for the flow past an idealized superhydrophobic flat surface is due to Philip [17]. He considered the wall composed by alternating stripes with no-slip and no-shear boundary conditions, both aligned and perpendicular to the flow direction, and derived an exact analytical expression for the protrusion heights using a method based on conformal mapping. More recently, Lauga and Stone [18] solved analytically the Stokes flow through circular channels with the same assumptions about the wall boundary conditions made by Philip. Even if the no-shear assumption is not valid in general at fluid-fluid interfaces, it is a reasonable approximation in the limit of vanishing viscosity ratio between the fluids in contact, as in the case of water flowing over an air layer. Under this assumption, Davis and Lauga [19] and Crowdy [20] extended the work by Philip, including the effect of the curvature of the interface between the lubricant and the working fluid. The solution is analytic, given in terms of power expansions of the protrusion angle which quantifies how much the interface is depressing into or protruding out of the wall cavities. Nevertheless, these studies are not free of limitations, since they are theoretically valid only for small extensions of the slip region (the so-called dilute limit). In any case, a comparison with numerical simulations by Hyväluoma and Harting [21], Sbragaglia and Prosperetti [22], and Teo and Khoo [23] demonstrated that the validity of the analytical model extends beyond the limitation under which the relations were derived. The first attempt to remove the restrictions related with the shear-free region extension is due to Ng and Wang [24], who also extended the work with

a semianalytical model for the longitudinal and transverse flow over a periodic array of circular and spherical protrusions, imposing a constant level of slip on the interface. The level of slip is rendered by using the relation (1), introducing an intrinsic slip length related to the interface. The solution is given in terms of a series, where unknown coefficients have to be found as function of the slip allowed. Some time later, with the same assumption on the interface boundary condition, Crowdy [25] extended the work of Ng and Wang [24] by finding an explicit approximation for the longitudinal slip length using a method based on spectral functions. The same author [26] also generalized the dilute-limit result of Davis and Lauga to arbitrary no-shear fractions. Schönecker *et al.* [27] were the first to explicitly take into account the effect of the viscosity ratio between the fluids in contact, providing an analytical expression for both the transverse and parallel slip lengths. Their formulas extended the relation provided by Belyaev and Vinogradova [28] valid only for very small viscosity ratios; they are, however, limited to only flat and rigid interfaces. Moreover in their paper they provided some important consideration on the effect of the pocket geometry on the protrusion heights. Ageev and Osiptsov [29] and Ageev *et al.* [30] very recently performed a simulation campaign to measure the value of the slip lengths for both the pressure-driven and the shear-driven flow in a superhydrophobic channel, taking into account different levels of filling of the gas trapped within the wall cavities. The results are given in terms of the ratio between the mean velocity and the mean derivative of the velocity at the surface, following the definition originally introduced by Navier [16]. Similarly, Li *et al.* [31] performed numerical simulations of SHSs in laminar channel flow using a *volume of fluid* model to treat the interface, studying the groove geometry, interface shear rate, and meniscus penetration effect on the effective slip length. They also provided an analytical model which correlates well with their simulations.

The computational works meant to quantify the drag reduction induced by an SHS or LIS is mainly based on direct numerical simulations (DNSs) of a classical turbulent channel with various levels of approximation for the boundary conditions at the walls. The first work was conducted by Min and Kim [32], who modeled the slip at the wall using the Navier boundary conditions. Their work highlighted the effect of the streamwise and spanwise slip, pointing out that a slip in the transverse direction enhances turbulence, contributing to a drag increase. However, the slip lengths were arbitrarily fixed, even if to reasonable values. Taking advantage of these results, Fukagata and Kasagi [33] proposed a theoretical model of friction drag reduction for arbitrary values of the slip lengths. Martell *et al.* [34] performed numerical simulations of a turbulent flow over SHSs using a variety of shear-free surface patters (longitudinal stripes or square posts) applied only at the bottom wall. The same authors later extended their previous work up to $\mathrm{Re}_\tau = 590$ [35]. In these cases the slip length was deduced as a results of the simulations, and drag reduction was measured. Busse and Sandham [36] extended the work of Min and Kim [32], performing a large number of simulations of a turbulent channel flow, exploring the influence of anisotropic slip-length boundary conditions. They also improved the analytical model proposed by Fukagata and Kasagi [33], obtaining an excellent agreement with their numerical simulations. Turk *et al.* [37] made an extensive analysis of the turbulent statistics and the secondary flows for a similar case with both channel walls coated with longitudinal ridges. Seo *et al.* [38] performed several DNSs at $\mathrm{Re}_\tau \approx 197$ and $\mathrm{Re}_\tau \approx 395$ using again posts or ridges at the wall where the no-shear condition was applied to mimic the superhydrophobic effect. They accounted also for the deformation of the interface together with the turbulent flow, by solving the Young-Laplace equation after the pressure distribution at the wall had been determined. Later the same authors [39] extended their work proposing a threshold criterion for the failure of superhydrophobic surfaces and boundary maps to identify stable and unstable zones in a parameter space consisting of working parameter and design parameters including texture size and material contact angle. The numerical simulations by Luchini [40] and Seo and Mani [41] demonstrated that the complete no-slip and no-shear boundary conditions give equivalent results in terms of drag reduction to the Navier boundary conditions, provided that the extension of the shear-free region does not exceed 20 wall units. This is a favorable result that allows one to employ a homogeneous treatment of the wall (i.e., the Navier boundary condition) without affecting the accuracy of the results. It is worth noting that the first studies simulating directly the liquid-air layer

are starting to appear [42] and can surely offer a detailed knowledge of the slipping phenomena over SHSs and LISs in turbulent flows.

Our aim is to propose a boundary element formulation to deal with both the longitudinal and transverse problems and able to recover the values of the slip lengths without approximations. In the following we take into account the viscosity ratio between the working and lubricant fluid, the curvature of the interface, and the geometric features of the wall grooves. Finally, a brief discussion on the applicability limit of the protrusion heights in the Navier boundary condition as a wall model for SHSs and LISs is offered on the basis of DNS results.

II. THE MICROSCOPIC PROBLEM

The velocity profile in the viscous sublayer near a wall of a turbulent boundary layer has been extensively studied from both numerical and experimental points of view, leading to an in-depth knowledge of the phenomena taking place in this thin, but important, region.

Our aim is to understand how a microcorrugated wall, with gas or oil cavities within, affects the viscous sublayer, in the directions both parallel and normal to the corrugations. Since in this region the convective terms are negligible, the equations reduce to

$$\boldsymbol{\nabla} p = \mu \nabla^2 \boldsymbol{u}, \quad \boldsymbol{\nabla} \cdot \boldsymbol{u} = 0. \tag{2}$$

The starting point consists in recognizing that two problems exist, an inner problem ruled by microscopic variables and an outer, macroscopic problem for which the bounding surface is smooth (and can be taken to coincide with the tips of the ribleted surface). The boundary behavior of the outer solution requires there to be a wall slip velocity, U_s, and a wall shear rate, $\kappa_w = \frac{\partial U}{\partial y}|_{y=0}$. In dimensionless terms, an outer wall-normal variable, Y, can be defined, related to the corresponding inner variable $\tilde{y}$ by

$$Y = \epsilon \tilde{y};$$

$\epsilon = b/L$ is a small parameter (with b the microscopic length scale and L the macroscale characterizing outer flow phenomena). The inner scales used to normalize the dimensional Stokes equations and the boundary conditions are b as length scale (see Fig. 1), $b\,\kappa_w$ as velocity scale, and $\mu\,\kappa_w$ as pressure scale. The shear rate is imposed by the outer solution onto the inner one so that, when the outer variable $Y \to 0$, the dimensional streamwise component of the velocity tends to $U_s + \kappa_w L Y$ (the spanwise component also behaves linearly in Y, by an analogous reasoning). Observe that in an asymptotic sense when $Y \to 0$ we have $\tilde{y} \to \infty$, and, in inner variables scalings, the streamwise velocity component $\tilde{u}$, in dimensionless form, tends to $\frac{U_s}{b\,\kappa_w} + \tilde{y}$:

$$\left.\frac{\partial \tilde{u}}{\partial \tilde{y}}\right|_{\tilde{y}\to\infty} \to 1.$$

Adopting the above normalization, the governing equations (Stokes plus continuity) read

$$\boldsymbol{\nabla} p = \nabla^2 \boldsymbol{u}, \quad \boldsymbol{\nabla} \cdot \boldsymbol{u} = 0; \tag{3}$$

there should be no ambiguity with the fact that, from now on, everything is nondimensional, although tildes have been removed from the variables' names.

In principle, the above is a three-dimensional system; however, it might be decoupled into two separate two-dimensional problems when corrugations homogeneous along the streamwise directions are considered. In order to apply this geometric constraint, we have to assume that the interface between the two fluids is allowed to deform only under the effect of the transverse flow, remaining homogeneous along the longitudinal direction. If this hypothesis is satisfied, the initial Stokes problem is split into two different parts, known as transverse and longitudinal problems, whose governing equations together with the appropriate boundary conditions are reported in Fig. 1.

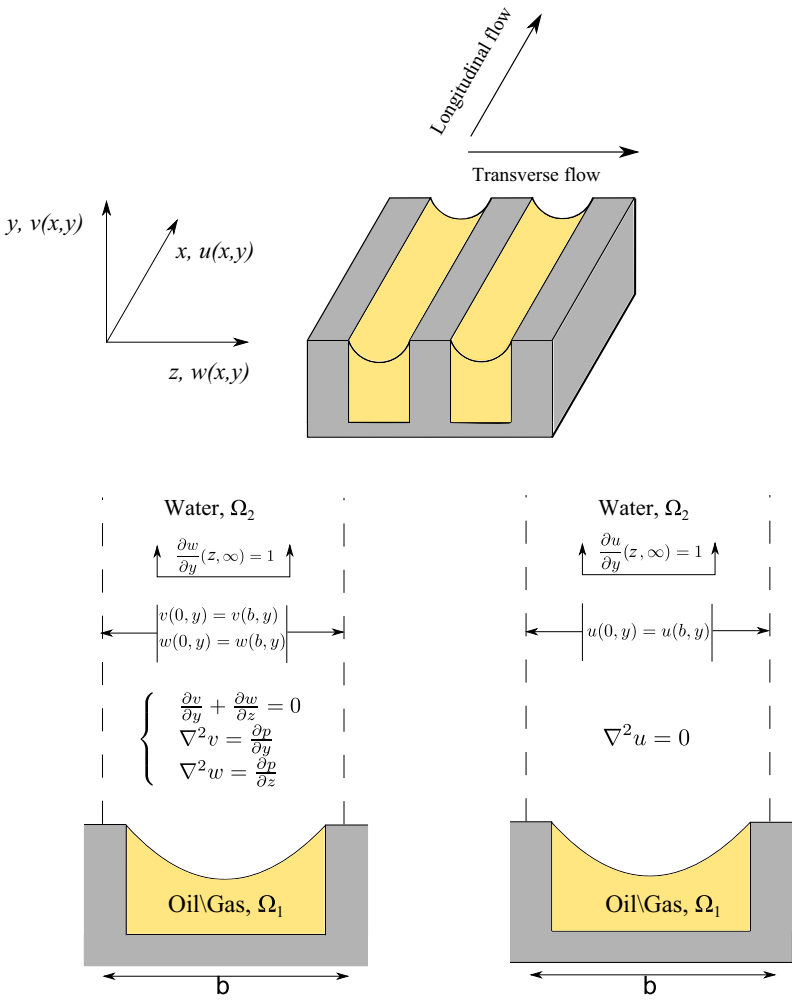

FIG. 1. Geometry, governing equations and boundary conditions for the transverse (bottom left) and the longitudinal (bottom right) problems.

In particular, the Laplace equation is found to govern the longitudinal flow, while the transverse and wall normal components of the velocity are described by a two-dimensional Stokes problem.

The linearity of the Laplace and the Stokes equations allows one to perform some analytical considerations on the behavior of the longitudinal and transverse velocity components. Far enough from the wall these components show a linear behavior [20] of the type

$$(u, w) = y + (h_{||}, h_{\perp}); \tag{4}$$

as already stated above, the two constants $h_{||}$ and $h_{\perp}$ will be called either protrusion heights or slip lengths and represent the two virtual distances below a reference surface where the velocity components extrapolate to zero. They need not coincide, aside from very particular isotropic wall patterns, and express by how much the actual wall impedes the flow along the longitudinal or the transverse direction [43]. One elegant way to deal with the longitudinal and transverse problems is to employ the boundary integral method (BIM), which is a powerful mathematical technique that allows one to recast an original differential problem into an integral one. In theory, there are no restrictions on the type of differential problem suitable for this transformation; however,

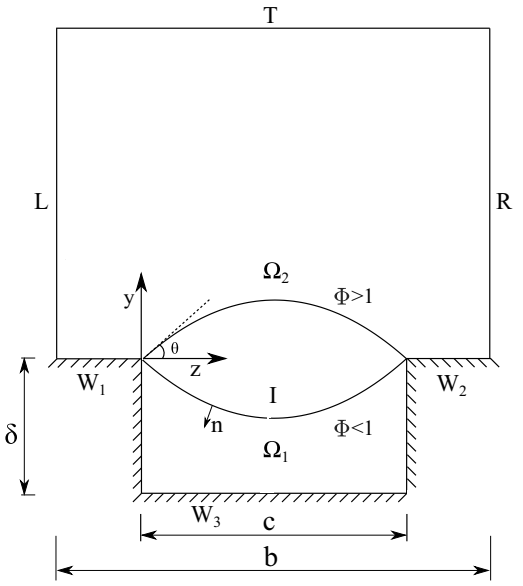

FIG. 2. Wall geometry for a depressing ($\Phi < 1$) or protruding ($\Phi > 1$) interface I.

the BIM is mostly applied to linear, elliptic, and homogeneous partial differential equations governing boundary-value problems. The key idea of this method is to express the solution in terms of boundary distributions of fundamental solutions of the differential equation considered. The fundamental solutions are Green's functions expressing the field due to a localized source and the densities of the distributions are then computed to satisfy the specified boundary conditions. Since the equations involved are the Laplace equation, governing the longitudinal problem, and the Stokes equation, governing the transverse problem, the BIM finds an effective applicability.

A. Parameters

We focus our attention on a particular geometry of the wall grooves which has been successfully employed for the artificial generation of SHSs and LISs (see, for example, Refs. [9,44]) and sketched in Fig. 2. There are several parameters which impact on the slipping properties of the surface and that need to be discussed more in detail. Starting from the geometrical parameters, the first is related to the periodicity of the groove, b. It is known from the seminal study by Philip [17] that the slip lengths depends on the value b, thus from a theoretical point of view a large spanwise periodicity of the grooves would be beneficial for the slipping performance of the surface. However, from a practical point of view, too largely spaced grooves might exhibit severe problems related to lubricant layer depletion. Once the periodicity is fixed, the free parameter is the extension of the fluid-lubricant interface, here denoted with c. It is clear that the larger the region of contact between the lubricant and the working fluid is, the smaller is the region where the no-slip condition applies, and this results in superior slipping properties. The last parameter related to the groove geometry is the depth of the lubricant layer δ. Its influence has been studied by Schönecker *et al.* [27], who figured out that it has a relevant effect only when the ratio $\frac{\delta}{c}$ is small (i.e., the wall cavity is much more wide than deep), otherwise the slip lengths are substantially independent from this parameter. Once the geometry of the wall cavity is fixed, the only geometric parameter left is associated with the interface, which can either protrude out or cave into the wall. We use $\Phi = \frac{V_l}{V_c} = 1 + \frac{\int_0^c y_0(z)\,dz}{c\delta}$, defined as the ratio of the volume of the lubricant fluid to the volume of the cavity, as a measure of the interface protrusion, with $y_0(z)$ the initial shape of the fluid interface. This choice is motivated by the fact that this

quantity is independent from the shape of the interface, by mass conservation. According to our definition, $\Phi > 1$ means that the meniscus is protruding outside of the cavity, while $\Phi < 1$ means that the meniscus caves into the wall; the flat interface is found when $\Phi = 1$. In our problem, we have two additional parameters related to the physical properties of the fluids in contact. The major effect on the slip lengths is given by the viscosity ratio $\lambda = \frac{\mu_l}{\mu_w}$, where μ_l and μ_w are the dynamic viscosities of the lubricant and the working fluid, respectively. If λ is very low, then the shear stress at the interface is negligible and slippage is maximized, but for other values, the effect is nontrivial. It has been studied by Schönecker *et al.* [27] in the approximation of a flat interface. Finally, the rigidity of the interface and thus its level of deformation is tuned by the capillary number $\mathrm{Ca} = \frac{\mu_w u_{\mathrm{ref}}}{\sigma}$, where σ is the surface tension and u_{ref} is a reference velocity that, for a turbulent flow, can be taken equal to the friction velocity $u_\tau = \sqrt{\tau_w/\rho}$, with τ_w the shear stress at wall and ρ the fluid density. For very low values of Ca the interface assumes a known shape function of the volume fraction Φ, as prescribed by the Young-Laplace equation. For $\Phi > 1$, the interface is an arc of a circle [19], while for $\Phi < 1$ the interface is described by a parabola [45]. As Ca increases the interface deforms nontrivially.

B. The microscopic longitudinal problem

We consider first the longitudinal flow over a periodic array of grooves aligned with the main flow direction. The Laplace equation holds in both the domains Ω_1 and Ω_2 and reads $\nabla^2 u = 0$. In order to take advantage of the boundary integral method, let us introduce the single-layer and the double-layer potentials for the Laplace equation, defined for a closed, two-dimensional, contour $\mathcal{C}$ as

$$\mathcal{F}^{\mathrm{SLP}}(\boldsymbol{x}_0, \nabla u \cdot \boldsymbol{n}; \mathcal{C}) = \int_{\mathcal{C}} G(\boldsymbol{x}, \boldsymbol{x_0})[\nabla u(\boldsymbol{x}) \cdot \boldsymbol{n}]\, dl(\boldsymbol{x}), \tag{5}$$

$$\mathcal{F}^{\mathrm{DLP}}(\boldsymbol{x}_0, u; \mathcal{C}) = \int_{\mathcal{C}} u(\boldsymbol{x})[\nabla G(\boldsymbol{x}, \boldsymbol{x_0}) \cdot \boldsymbol{n}]\, dl(\boldsymbol{x}), \tag{6}$$

where $\boldsymbol{x}_0$ is the generic field point, $\boldsymbol{n}$ is the normal vector to the contour $\mathcal{C}$, pointing inward the domain, and $G(\boldsymbol{x}, \boldsymbol{x}_0)$ is the Green function for the two-dimensional Laplace equation. The basic idea is to derive one boundary integral equation, linking the fluid quantities at the boundary of the domain using the operators (5) and (6), for each patch composing the geometry under investigation, that in our case is sketched in Fig. 2. Maintaining the usual convention of the boundary integral method, all the normal vectors $\boldsymbol{n}$ defined over the patches point inward the respective domain; since the interface is shared between both the domains, we choose its normal pointing inward the domain Ω_1 (see Fig. 2), and, thus, the relation $\boldsymbol{n}^{(2)} = -\boldsymbol{n}^{(1)}$ holds on I.

The starting point to derive the longitudinal flow integral representation is to apply the boundary integral formulation [46] in the lower fluid [superscript (1)] for a point $\boldsymbol{x}_0$ located at the interface I, which reads

$$\frac{u^{(1)}}{2} = -\mathcal{F}^{\mathrm{SLP}}(\boldsymbol{x}_0, \nabla u^{(1)} \cdot \boldsymbol{n}; \mathsf{W}_3) - \mathcal{F}^{\mathrm{SLP}}(\boldsymbol{x}_0, \nabla u^{(1)} \cdot \boldsymbol{n}^{(1)}; \mathsf{I}) + \hat{\mathcal{F}}^{\mathrm{DLP}}(\boldsymbol{x}_0, u^{(1)}; \mathsf{I}), \tag{7}$$

where $\hat{\mathcal{F}}^{\mathrm{DLP}}$ denotes the principal value of the double layer potential and the superscript is retained only in the normal vector defined over the interface to recall that in this case they are of opposite sign, while for the other cases it is implicitly assumed that the normal vector follows the convection described above. Repeating the derivation in the upper fluid [superscript (2)] for a point $\boldsymbol{x}_0$ located at the interface, we obtain

$$\begin{aligned}\frac{u^{(2)}}{2} = &-\mathcal{F}^{\mathrm{SLP}}(\boldsymbol{x}_0, \nabla u^{(2)} \cdot \boldsymbol{n}; \mathsf{W}_1 + \mathsf{W}_2 + \mathsf{T}) + \mathcal{F}^{\mathrm{DLP}}(\boldsymbol{x}_0, u^{(2)}; \mathsf{T}) \\ &- \mathcal{F}^{\mathrm{SLP}}(\boldsymbol{x}_0, \nabla u^{(2)} \cdot \boldsymbol{n}^{(2)}; \mathsf{I}) + \hat{\mathcal{F}}^{\mathrm{DLP}}(\boldsymbol{x}_0, u^{(2)}; \mathsf{I}).\end{aligned} \tag{8}$$

It is worth noting that the contributions of the periodic boundaries L and R cancel out from the integral equations if a suitable Green's function for the Laplace equation [46] is employed during the derivations. Since the velocity is assumed continuous across the interface, we add Eq. (7), multiplied by the viscosity ratio $\lambda = \frac{\mu_l}{\mu_w}$, to Eq. (8), and we collect the terms involving the velocity at the interface. The multiplication by λ is necessary to introduce in the final boundary integral equation the dependence from this parameter. Proceeding as illustrated, the first boundary integral equation reads

$$\frac{1+\lambda}{2}u(\boldsymbol{x}_0) = \mathcal{F}^{\mathrm{DLP}}(\boldsymbol{x}_0, u; \mathsf{T}) - \lambda\mathcal{F}^{\mathrm{SLP}}(\boldsymbol{x}_0, \nabla u \cdot \boldsymbol{n}; \mathsf{W}_3) - \mathcal{F}^{\mathrm{SLP}}(\boldsymbol{x}_0, \nabla u \cdot \boldsymbol{n}; \mathsf{W}_1 + \mathsf{W}_2 + \mathsf{T}) + \mathcal{F}^{\mathrm{SLP}}(\boldsymbol{x}_0, [\nabla u^{(2)} - \lambda \nabla u^{(1)}] \cdot \boldsymbol{n}; \mathsf{I}) + (\lambda - 1)\hat{\mathcal{F}}^{\mathrm{DLP}}(\boldsymbol{x}_0, u; \mathsf{I}), \tag{9}$$

with the interface unit normal vector $\boldsymbol{n}$ taken to coincide with $\boldsymbol{n}^{(1)}$.

Next, we consider the equation for the velocity in the lower fluid for a point $\boldsymbol{x}_0$ at the lower wall, multiplied by λ, together with the reciprocal relation for the Laplace equation [46]:

$$\frac{\lambda}{2}u^{(1)} = -\lambda\mathcal{F}^{\mathrm{SLP}}(\boldsymbol{x}_0, \nabla u^{(1)} \cdot \boldsymbol{n}; \mathsf{W}_3) - \lambda\mathcal{F}^{\mathrm{SLP}}(\boldsymbol{x}_0, \nabla u^{(1)} \cdot \boldsymbol{n}^{(1)}; \mathsf{I}) + \lambda\mathcal{F}^{\mathrm{DLP}}(\boldsymbol{x}_0, u^{(1)}; \mathsf{I}), \tag{10}$$

$$-\mathcal{F}^{\mathrm{SLP}}(\boldsymbol{x}_0, \nabla u^{(2)} \cdot \boldsymbol{n}; \mathsf{W}_1 + \mathsf{W}_2 + \mathsf{T}) + \mathcal{F}^{\mathrm{DLP}}(\boldsymbol{x}_0, u^{(2)}; \mathsf{T}) - \mathcal{F}^{\mathrm{SLP}}(\boldsymbol{x}_0, \nabla u^{(2)} \cdot \boldsymbol{n}^{(2)}; \mathsf{I}) + \mathcal{F}^{\mathrm{DLP}}(\boldsymbol{x}_0, u^{(2)}; \mathsf{I}) = 0. \tag{11}$$

We move the term composing Eq. (11) from the left-hand side to the right-hand side, and then we change its sign; adding the result of this manipulation to Eq. (10), we end up with

$$0 = \mathcal{F}^{\mathrm{DLP}}(\boldsymbol{x}_0, u; \mathsf{T}) - \lambda\mathcal{F}^{\mathrm{SLP}}(\boldsymbol{x}_0, \nabla u \cdot \boldsymbol{n}; \mathsf{W}_3) - \mathcal{F}^{\mathrm{SLP}}(\boldsymbol{x}_0, \nabla u \cdot \boldsymbol{n}; \mathsf{W}_1 + \mathsf{W}_2 + \mathsf{T}) + \mathcal{F}^{\mathrm{SLP}}(\boldsymbol{x}_0, [\nabla u^{(2)} - \lambda \nabla u^{(1)}] \cdot \boldsymbol{n}; \mathsf{I}) + (\lambda - 1)\mathcal{F}^{\mathrm{DLP}}(\boldsymbol{x}_0, u; \mathsf{I}), \tag{12}$$

where the zero on the left-hand side is due to the fact that the no-slip boundary condition is applied at the solid walls. The same equation can be derived for a point $\boldsymbol{x}_0$ belonging to the walls W_1 and W_2 by writing the equation for the upper fluid and the reciprocal relation, using as integration path the lower fluid domain, again multiplied by λ.

Finally, we apply the boundary integral formulation for a point $\boldsymbol{x}_0$ on the upper wall, and the reciprocal relation, multiplied by λ, obtaining

$$\frac{u^{(2)}}{2} = -\mathcal{F}^{\mathrm{SLP}}(\boldsymbol{x}_0, \nabla u^{(2)} \cdot \boldsymbol{n}; \mathsf{W}_1 + \mathsf{W}_2 + \mathsf{T}) + \mathcal{F}^{\mathrm{DLP}}(\boldsymbol{x}_0, u^{(2)}; \mathsf{T}) - \mathcal{F}^{\mathrm{SLP}}(\boldsymbol{x}_0, \nabla u^{(2)} \cdot \boldsymbol{n}^{(2)}; \mathsf{I}) + \mathcal{F}^{\mathrm{DLP}}(\boldsymbol{x}_0, u^{(2)}; \mathsf{I}), \tag{13}$$

$$-\lambda\mathcal{F}^{\mathrm{SLP}}(\boldsymbol{x}_0, \nabla u^{(1)} \cdot \boldsymbol{n}; \mathsf{W}_3) - \lambda\mathcal{F}^{\mathrm{SLP}}(\boldsymbol{x}_0, \nabla u^{(1)} \cdot \boldsymbol{n}; \mathsf{I}) + \lambda\mathcal{F}^{\mathrm{DLP}}(\boldsymbol{x}_0, u^{(1)}; \mathsf{I}) = 0. \tag{14}$$

Summing Eqs. (13) and (14) and performing similar manipulations as in Eq. (11), we obtain the last boundary integral equation

$$\tfrac{1}{2}u(\boldsymbol{x}_0) = \hat{\mathcal{F}}^{\mathrm{DLP}}(\boldsymbol{x}_0, u; \mathsf{T}) - \lambda\mathcal{F}^{\mathrm{SLP}}(\boldsymbol{x}_0, \nabla u \cdot \boldsymbol{n}; \mathsf{W}_3) - \mathcal{F}^{\mathrm{SLP}}(\boldsymbol{x}_0, \nabla u \cdot \boldsymbol{n}; \mathsf{W}_1 + \mathsf{W}_2 + \mathsf{T}) + \mathcal{F}^{\mathrm{SLP}}(\boldsymbol{x}_0, [\nabla u^{(2)} - \lambda \nabla u^{(1)}] \cdot \boldsymbol{n}; \mathsf{I}) + (\lambda - 1)\mathcal{F}^{\mathrm{DLP}}(\boldsymbol{x}_0, u; \mathsf{I}), \tag{15}$$

which forms, together with (9) and (12), a system of integral equations for the unknown velocity or stress distribution along the domain's boundaries. The formulation undergoes a further simplification if the jump in shear stress across the interface, $[\nabla u^{(2)} - \lambda \nabla u^{(1)}] \cdot \boldsymbol{n}$, along the longitudinal

direction is specified. In this particular problem we require $\nabla u^{(2)} \cdot \boldsymbol{n} = \lambda \nabla u^{(1)} \cdot \boldsymbol{n}$, i.e., we assume the shear stress to be continuous across the interface.

Once the velocity and its gradient are know at the boundaries, the internal field can be readily reconstructed by using the following integral relation:

$$\begin{aligned}\alpha u(\boldsymbol{x}_0) = &-\lambda \mathcal{F}^{\mathrm{SLP}}(\boldsymbol{x}_0, \nabla u \cdot \boldsymbol{n}; \mathsf{W}_3) - \mathcal{F}^{\mathrm{SLP}}(\boldsymbol{x}_0, \nabla u \cdot \boldsymbol{n}; \mathsf{W}_1 + \mathsf{W}_2 + \mathsf{T}) \\ &+ \mathcal{F}^{\mathrm{DLP}}(\boldsymbol{x}_0, u; \mathsf{T}) + (\lambda - 1)\mathcal{F}^{\mathrm{DLP}}(\boldsymbol{x}_0, u; \mathsf{I}),\end{aligned} \tag{16}$$

with

$$\begin{aligned}\alpha &= \lambda, \quad \text{if} \quad \boldsymbol{x}_0 \in \Omega_1, \\ \alpha &= 1, \quad \text{if} \quad \boldsymbol{x}_0 \in \Omega_2.\end{aligned}$$

C. The microscopic transverse problem

Following a similar procedure, we derive the governing integral equations for the transverse problem, involving the wall normal and the spanwise components of the velocity vector, denoted by $\boldsymbol{v} = (w, v)$. We first introduce the single-layer and the double-layer potential for the Stokes flow, which read

$$\mathcal{F}_j^{\mathrm{SLP}}(\boldsymbol{x}_0, \boldsymbol{f}; \mathcal{C}) = \frac{1}{4\pi\mu} \int_{\mathcal{C}} f_i(\boldsymbol{x}) \boldsymbol{G}_{ij}(\boldsymbol{x}, \boldsymbol{x_0})\, dl(\boldsymbol{x}), \tag{17}$$

$$\mathcal{F}_j^{\mathrm{DLP}}(\boldsymbol{x}_0, \boldsymbol{v}; \mathcal{C}) = \frac{1}{4\pi} \int_{\mathcal{C}} v_i(\boldsymbol{x}) \boldsymbol{T}_{ijk}(\boldsymbol{x}, \boldsymbol{x_0}) n_k(\boldsymbol{x})\, dl(\boldsymbol{x}). \tag{18}$$

A step-by-step derivation of the governing integral equations is found in Alinovi and Bottaro [45]; here we repropose for completeness their final form, which is employed in solving the transverse problem:

$$\begin{aligned}\frac{1+\lambda}{2} v_j(\boldsymbol{x}_0) = &-\mathcal{F}_j^{\mathrm{SLP}}(\boldsymbol{x}_0, \boldsymbol{f}; \mathsf{W} + \mathsf{T}) + \mathcal{F}_j^{\mathrm{DLP}}(\boldsymbol{x}_0, \boldsymbol{v}; \mathsf{T}) \\ &- \mathcal{F}_j^{\mathrm{SLP}}(\boldsymbol{x}_0, \Delta \boldsymbol{f}; \mathsf{I}) + (\lambda - 1)\hat{\mathcal{F}}_j^{\mathrm{DLP}}(\boldsymbol{x}_0, \boldsymbol{v}; \mathsf{I}),\end{aligned} \tag{19}$$

$$\begin{aligned}\frac{v_j(\boldsymbol{x}_0)}{2} = &-\mathcal{F}_j^{\mathrm{SLP}}(\boldsymbol{x}_0, \boldsymbol{f}; \mathsf{W} + \mathsf{T}) - \mathcal{F}_j^{\mathrm{SLP}}(\boldsymbol{x}_0, \boldsymbol{f}; \mathsf{T}) + \mathcal{F}_j^{\mathrm{DLP}}(\boldsymbol{x}_0, \boldsymbol{v}; \mathsf{T}) \\ &- \mathcal{F}_j^{\mathrm{SLP}}(\boldsymbol{x}_0, \Delta \boldsymbol{f}; \mathsf{I}) + (\lambda - 1)\mathcal{F}_j^{\mathrm{DLP}}(\boldsymbol{x}_0, \boldsymbol{v}; \mathsf{I}) = 0,\end{aligned} \tag{20}$$

$$\begin{aligned}\frac{v_j(\boldsymbol{x}_0)}{2} = &-\mathcal{F}_j^{\mathrm{SLP}}(\boldsymbol{x}_0, \boldsymbol{f}; \mathsf{W} + \mathsf{T}) - \mathcal{F}_j^{\mathrm{SLP}}(\boldsymbol{x}_0, \boldsymbol{f}; \mathsf{T}) + \hat{\mathcal{F}}_j^{\mathrm{DLP}}(\boldsymbol{x}_0, \boldsymbol{v}; \mathsf{T}) \\ &- \mathcal{F}_j^{\mathrm{SLP}}(\boldsymbol{x}_0, \Delta \boldsymbol{f}; \mathsf{I}) + (\lambda - 1)\mathcal{F}_j^{\mathrm{DLP}}(\boldsymbol{x}_0, \boldsymbol{v}; \mathsf{I}).\end{aligned} \tag{21}$$

Equations (19)–(21) are a system of integral equations for the unknown stresses along the solid walls, the interface velocity, and the velocity or the stress on the top boundary T, as function of the applied boundary conditions. The internal velocity field can be reconstructed using

$$\begin{aligned}\alpha v_j(\boldsymbol{x}_0) = &-\mathcal{F}_j^{\mathrm{SLP}}(\boldsymbol{x}_0, \boldsymbol{f}; \mathsf{W} + \mathsf{T}) - \mathcal{F}_j^{\mathrm{SLP}}(\boldsymbol{x}_0, \boldsymbol{f}; \mathsf{T}) + \mathcal{F}_j^{\mathrm{DLP}}(\boldsymbol{x}_0, \boldsymbol{v}; \mathsf{T}) \\ &- \mathcal{F}_j^{\mathrm{SLP}}(\boldsymbol{x}_0, \Delta \boldsymbol{f}; \mathsf{I}) + (\lambda - 1)\mathcal{F}_j^{\mathrm{DLP}}(\boldsymbol{x}_0, \boldsymbol{v}; \mathsf{I}),\end{aligned} \tag{22}$$

with

$$\begin{aligned}\alpha &= \lambda, \quad \text{if} \quad \boldsymbol{x}_0 \in \Omega_1, \\ \alpha &= 1, \quad \text{if} \quad \boldsymbol{x}_0 \in \Omega_2.\end{aligned}$$

The nondimensional jump in traction through the interface due to the surface tension is $\Delta \boldsymbol{f} = \boldsymbol{f}^{(1)} - \boldsymbol{f}^{(2)} = \frac{K\boldsymbol{n}}{\mathrm{Ca}}$, with Ca the capillary number, $\mathrm{Ca} = \frac{\mu_w u_{\mathrm{ref}}}{\sigma}$, and K the local curvature of the interface.

D. Numerical method

The integral equations described in the previous sections are not amenable to analytical solution due to the complexity of the integral operators. The common practice to obtain a solution is to employ the boundary element method (BEM). The BEM is the numerical counterpart of BIM and consists in subdividing the boundary of the domain into a collection of discrete elements. The shape of the elements is important in order to obtain an accurate representation of the boundary with a low number of elements to minimize the computational efforts. The simplest option is to approximate the boundary with a set of straight segments, while more involved solutions require the usage of high order spline approximations. The elements' shape is not the only choice to be made, since also the boundary quantities in the integrals have to be somehow estimated. The simplest option is to consider constant the integrand function over each element, but in this case a large number of elements must be employed if an accurate solution is needed. A higher order approximation based on polynomial interpolants is often used to obtain a more accurate solution with a lower resolution.

Our choice is to use a superparametric BEM, which has a good balance between accuracy and difficulty of implementation. We employ a linear approximation for the boundary quantities and cubic splines for the interface in order to have a good approximation of the curved boundary. For a detailed description of the numerical method, the reader can refer to Alinovi and Bottaro [45]; here we proceed to the discretization of the governing integral equation, without specifying any type of approximation for either the discrete elements or the boundary quantities, leading to a general numerical discretization. Independently from the type of BEM, its main advantage is that it is not necessary to compute the required functions throughout the domain of solution. Once the unknown boundary distribution is available, the solution at any point may be produced by direct evaluation. Thus, the key of the BEM is the reduction of the dimension of the solution space with respect to the physical space.

Let us proceed to the discretization and thus define with N_T, $N_W = N_{W_1} + N_{W_2} + N_{W_3}$, and N_I the number of the collocation points distributed along the top boundary, the lower wall and the interface, respectively; we identify with $\mathsf{W} = \mathsf{W}_1 + \mathsf{W}_2 + \mathsf{W}_3$ all the patches composing the lower wall. The integral equations in their discrete form for the longitudinal problem read

$$
\begin{aligned}
&-\boldsymbol{D}^{TT}\cdot\boldsymbol{u}^T + \frac{1}{2}\boldsymbol{u}^T + \boldsymbol{S}^{TW_{1,2}}\cdot\boldsymbol{u}_n^{W_{1,2}} + \lambda\boldsymbol{S}^{TW_3}\cdot\boldsymbol{u}_n^{W_3} - (\lambda-1)\boldsymbol{D}^{TI}\cdot\boldsymbol{u}^I = -\boldsymbol{S}^{TT}\cdot\boldsymbol{u}_n^T - \boldsymbol{S}^{TI}\cdot\Delta\boldsymbol{u}_n^I,\\
&-\boldsymbol{D}^{WT}\cdot\boldsymbol{u}^T - (\lambda-1)\boldsymbol{D}^{WI}\cdot u^I + \lambda\boldsymbol{S}^{WW_3}\cdot\boldsymbol{u}_n^{W_3} + \boldsymbol{S}^{WW_{1,2}}\cdot\boldsymbol{u}_n^{W_{1,2}} = -\boldsymbol{S}^{WT}\cdot\boldsymbol{u}_n^T - \boldsymbol{S}^{WI}\cdot\Delta\boldsymbol{u}_n^I,\\
&-\boldsymbol{D}^{IT}\cdot\boldsymbol{u}^T + \lambda\boldsymbol{S}^{IW_3}\cdot\boldsymbol{u}_n^{W_3} + \boldsymbol{S}^{IW_{1,2}}\cdot\boldsymbol{u}_n^{W_{1,2}} - (\lambda-1)\boldsymbol{D}^{II}\cdot\boldsymbol{u}^I + \frac{1+\lambda}{2}\boldsymbol{u}^I\\
&\quad = -\boldsymbol{S}^{IT}\cdot\boldsymbol{u}_n^T - \boldsymbol{S}^{II}\cdot\Delta\boldsymbol{u}_n^I,
\end{aligned}
\tag{23}
$$

while for the transverse problem,

$$
\begin{aligned}
&-\boldsymbol{D}^{TT}\cdot\boldsymbol{v}^T + \frac{1}{2}\boldsymbol{v}^T + \boldsymbol{S}^{TW}\cdot\boldsymbol{f}^W - (\lambda-1)\boldsymbol{D}^{TI}\cdot\boldsymbol{v}^I = -\boldsymbol{S}^{TT}\cdot\boldsymbol{f}^T - \boldsymbol{S}^{TI}\cdot\Delta\boldsymbol{f}^I,\\
&-\boldsymbol{D}^{WT}\cdot\boldsymbol{v}^T - (\lambda-1)\boldsymbol{D}^{WI}\cdot\boldsymbol{v}^I + \boldsymbol{S}^{WW}\cdot\boldsymbol{f}^W = -\boldsymbol{S}^{WT}\cdot\boldsymbol{f}^T - \boldsymbol{S}^{WI}\cdot\Delta\boldsymbol{f}^I,\\
&-\boldsymbol{D}^{IT}\cdot\boldsymbol{v}^T + \boldsymbol{S}^{IW}\cdot\boldsymbol{f}^W - (\lambda-1)\boldsymbol{D}^{II}\cdot\boldsymbol{v}^I + \frac{1+\lambda}{2}\boldsymbol{v}^I = -\boldsymbol{S}^{IT}\cdot\boldsymbol{f}^T - \boldsymbol{S}^{II}\cdot\Delta\boldsymbol{f}^I.
\end{aligned}
\tag{24}
$$

The quantity $\boldsymbol{u}_n$ is shorthand notation for scalar product $\nabla\boldsymbol{u}\cdot\boldsymbol{n}$, while $\Delta\boldsymbol{u}_n = [\lambda\nabla u^{(1)} - \nabla u^{(2)}]\cdot\boldsymbol{n}$ is the jump in shear stress across the interface and along the longitudinal direction; the matrices $\boldsymbol{S}$ and $\boldsymbol{D}$ are called influence matrices and are the discretized counterparts of the single-layer and

TABLE I. Size of the discretized single-layer operator.

$\boldsymbol{S}^{TT}$	$2N_T \times 2N_T$	$\boldsymbol{S}^{WI}$	$2N_W \times 2N_I$
$\boldsymbol{S}^{WT}$	$2N_W \times 2N_T$	$\boldsymbol{S}^{WW}$	$2N_W \times 2N_W$
$\boldsymbol{S}^{TW}$	$2N_T \times 2N_W$	$\boldsymbol{S}^{IT}$	$2N_I \times 2N_T$
$\boldsymbol{S}^{TI}$	$2N_T \times 2N_I$	$\boldsymbol{S}^{IW}$	$2N_I \times 2N_W$
$\boldsymbol{S}^{WT}$	$2N_W \times 2N_T$	$\boldsymbol{S}^{II}$	$2N_I \times 2N_I$

the double-layer potential operators defined in Eqs. (17) and (18). The first letter in the superscript denotes the position of the collocation point, while the second letter identifies the piece of boundary over which the integral operator is being evaluated. Since the matrices $\boldsymbol{D}^{**}$ have the same size of the corresponding matrices $\boldsymbol{S}^{**}$, only the size of the matrices $\boldsymbol{S}^{**}$ is reported in Table I. Regarding the expression of the coefficients of $\boldsymbol{S}$ and $\boldsymbol{D}$, they strictly depend on the shape and the order of the interpolation of the boundary quantities along the elements.

If the longitudinal problem is being considered, the size of the operators reported in Table I is to be divided by a factor of 4, since the field has only one component.

The interface has to be advanced in time in order to find its steady-state position, prescribed by the physical parameters involved in the simulation. Since we have assumed that there is no deformation along the longitudinal direction, then the interfaces are to be updated in time only along the transverse directions. In doing so, the boundary element method presents notable advantages with respect to other interface-tracking techniques, since we can easily perform an accurate Lagrangian tracking of the interface, using the collocation points employed for the discretization. Here they are advanced in time using the rule

$$\frac{d\boldsymbol{x}^{(i)}}{dt} = (\boldsymbol{u}_i \cdot \boldsymbol{n}_i)\boldsymbol{n}_i, \quad i = 1, \ldots, N_I, \tag{25}$$

where $\boldsymbol{x}^{(i)}$ is the ith collocation point and $\boldsymbol{n}_i$ is the normal to the interface at $\boldsymbol{x}^{(i)}$. Using the normal velocity to advance the interface, instead of the velocity $\boldsymbol{u}$, is found to be very effective in limiting the spreading of the collocation points, with the consequent advantage that the interface does not need to be frequently remeshed. Equation (25) can be discretized with any explicit scheme for ordinary differential equations. We have implemented both the first-order Euler and the second-order Runge-Kutta integration, finding negligible differences between the two schemes.

Once the interface reaches a steady state in the transverse problem, the shape of the interface is used in the computation of the longitudinal problem. The solution of the microscopic equations is carried out in a domain of spanwise dimension b equal to one and vertical dimension sufficiently large for the asymptotic solution to be established (the upper boundary can safely be taken at any value of y_∞ larger than 4 for the solution to become uniform there). The calculation of the slip lengths takes advantage of the asymptotic relations (4) for the velocity components, which are directly measured by our numerical code at $y = y_\infty$ (i.e., in correspondence of patch T). The dimensionless protrusion heights are then simply

$$(h_{||}, h_\perp) = [u(\infty) - y_\infty, w(\infty) - y_\infty]. \tag{26}$$

E. Comparison with previous work

The flow over superhydrophobic surfaces has been extensively studied from the theoretical point of view, assuming that on the interface perfect slip applies. This is a reasonable hypothesis only in the case of a very small viscosity ratio between the working fluid and the lubricant fluid. Our aim in this section is to compare the values of the protrusion heights coming from boundary element simulations with two analytical models proposed by Davis and Lauga [19] for the transverse problem and by Crowdy [20] for the longitudinal problem. The simulations are conducted using the air-water viscosity ratio in order to have a value low enough to consider the no-shear boundary

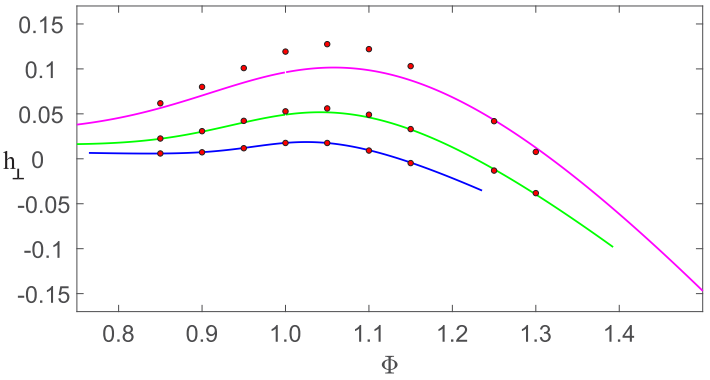

FIG. 3. Comparison in transverse protrusion heights (scaled by b) between the analytical model by Davis and Lauga [19] and the present numerical simulations. The solid lines correspond to the analytical model by Davis and Lauga for $c = 0.30$ (lower line), $c = 0.50$ (intermediate line), and $c = 0.70$ (upper line). Filled circles denote results of the present simulations, for the same values of c, with $\lambda = 0.018$ at $\mathrm{Ca} = 0.1$.

condition on the interface a reasonable approximation, thus making the results comparable. We start by considering the transverse problem, governed by the Stokes equation applied to the geometry in Fig. 2; we do not fix the interface's position and let the solution reach the steady state by updating the points on the interface as time advances. The mass conservation is enforced using a Lagrange multiplier approach [45], which is mandatory in order to obtain a mass-satisfying solution in the presence of viscosity ratios $\lambda < 1$. We have computed the slip length by varying the length of the cavity, c, and the volume ratio, Φ. In Fig. 3 we propose a comparison between the analytical model and our numerical simulations. The agreement is good, especially for the values $c = 0.30$ and $c = 0.50$, but this is not surprising, since the analytical model is valid in the limit of small values of c. If one compares the value of the slip length with $c = 0.70$ and flat interface ($\Phi = 1$), the model by Davis and Lauga [19] yields $h_\perp = 0.0963$ (the protrusion heights are normalized with b), while both Philip's and our calculations give $h_\perp = 0.126$. Increasing the viscosity ratio λ has the effect of decreasing the slip length, since for small λ the approximation of perfect slip along the interface is better. We will return to the effect of the viscosity ratio in the following section with a more extensive discussion. The present simulations also confirm the existence of a critical value of Φ for which the slip length becomes negative. This condition, already pointed out by Steinberger *et al.* [47] and Sbragaglia and Prosperetti [22], occurs when the interface has an excessive protrusion outside of the cavity. The largest value of the protrusion height is found, almost independently of Ca and λ, when Φ is close to 1.05, i.e., when the interface is very mildly protruding out of the cavity. The definite answer on the drag-reducing abilities of the surface can, however, come only from the resolution of the companion problem for the longitudinal protrusion height since, as shown by Luchini *et al.* [43], shear stress reduction at the wall depends to first order on the difference between longitudinal and transverse protrusion heights.

In the longitudinal problem case we reproduce exactly the setup found in the literature, since here there is no time advancing of the interface and any shape can be set. Figure 4 reports the comparisons between our numerical simulations, the analytical model by Crowdy [20], and the finite element calculations by Teo and Khoo [23], for the air-water viscosity ratio. Even in this case the results are in excellent agreement with the reference data, fitting very well both the analytical and the numerical predictions; the curve at $c = 0.75$ is slightly above the values calculated by our simulations, simply because the span of the interface is large and the effect of the nonzero viscosity ratio is mildly felt. The analytical approximation by Crowdy [20] gives very good result for $c < 0.50$; beyond this value of c the difference between the numerical and the analytical results become large and the analytical model is no longer applicable.

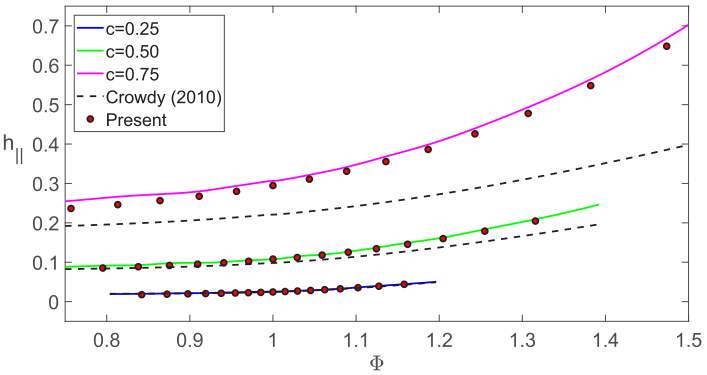

FIG. 4. Comparison in longitudinal protrusion heights (scaled by b) between the analytical model by Crowdy [20] (dashed lines), the numerical results by Teo and Khoo [23] (solid lines), and the present numerical simulations (filled circles) for different values of c at $\lambda = 0.018$.

F. Results for other viscosity ratios

In this section we compare the values of the slip lengths for both the longitudinal and transverse problems, as a function of salient geometrical and physical parameters. For our simulation campaign, we set the thickness of the lubricant cavity $\delta = 0.50$ and let c assume three different values of increasing magnitude, respectively, 0.30, 0.50, and 0.70. The interface is either depressing into or protruding out of the wall cavity as function of the volume fraction, Φ. The viscosity ratio λ between the lubricant and the working fluid is varied from low to high values, keeping in mind that $\lambda < 1$ is commonly encountered in gas-water situations (e.g., for air-water $\lambda = 0.018$), while $\lambda > 1$ belongs to oil lubricants. In particular it can be found that $\lambda = 20$–100 is commonly encountered for silicon oils [48], while $\lambda = 25$–50 is characteristic of vaseline oils [49], considering water as the working fluid. The capillary number tunes the stiffness of the interface, and, in practical applications, it is usually low enough to guarantee an almost rigid interface, undeformed with respect to the shape that would be assumed without flow forcing. In this situation, the interface is described by an arc of a circle for the case of a protruding bubble [19], while a parabolic shape occurs when the lubricant fluid is depressing into the wall cavity. During our simulations, we have found that values of $\mathrm{Ca} = 0.25$ and larger guarantee a substantially rigid interface, with very small deviation with respect to the steady-state position. This is a favorable result which permits avoiding the use of very small values of Ca, which may create an instability of the interface with the explicit time-advancing scheme used. Moreover, we found that the protrusion heights exhibit a very low dependency on the capillary number if it is set low enough to guarantee a stiff interface. The reason behind this result is that the value of the protrusion height is mainly influenced by the shape of the interface, which does not vary significantly for $\mathrm{Ca} > 0.25$. Due to these considerations, a value $\mathrm{Ca} = 0.1$ is employed in our calculations.

We start our analysis by comparing the computed longitudinal and transverse protrusion heights for different viscosity ratios and interface spans, which are the most significant parameters involved in the problem. In Fig. 5 the trend of the protrusion heights is shown against the volume fraction Φ. The perpendicular protrusion height $h_\perp$, reported in the left column, depends on the viscosity ratio; its magnitude increases with both λ and c. The physical interpretation is straightforward: on the one hand, the slippage over the lubricant film is promoted by a low value of the viscosity ratio, and, on the other, the working fluid encounters a lower resistance as the portion of no-slip wall is decreased. Moreover, we note that the reduction in magnitude, associated with the increase of the lubricant fluid viscosity, is not linear, and, for example, an increase of λ from 0.018 to 0.1 produces a small drop in protrusion height, with the two curves which remain quite close, especially for the lower value of c. In Fig. 5 we have reported also the analytical values of the

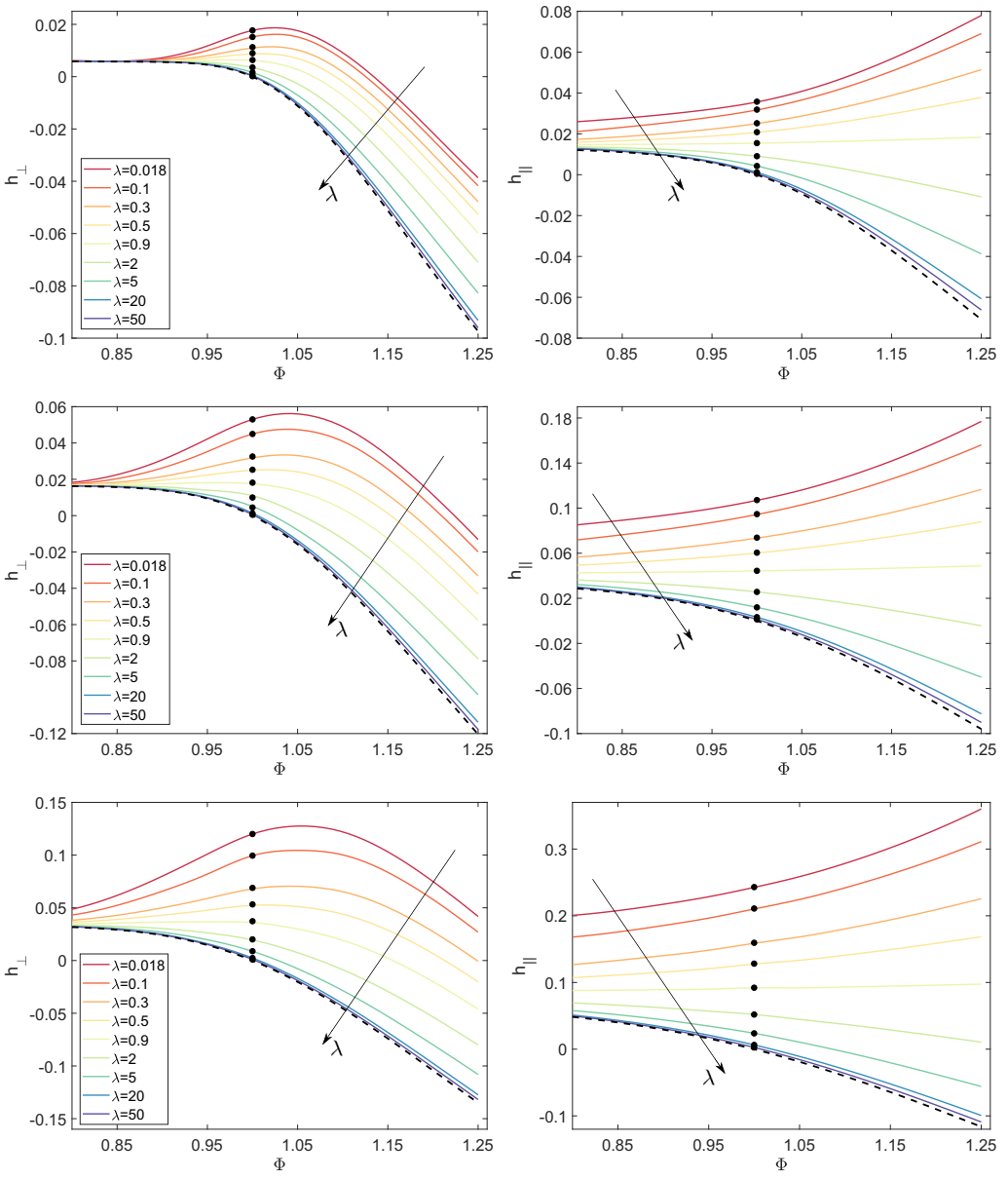

FIG. 5. Computed transverse (left column) and longitudinal protrusion heights for increasing values of c and a wide range of λ, increasing according to the direction of the arrow, at $\mathrm{Ca} = 0.1$. The value of the interface span c is increased from top to bottom, namely, $c = 0.30$ in the top row, $c = 0.50$ in the middle row, and $c = 0.70$ in the bottom row. The dashed lines illustrate the values of the protrusion heights when $\lambda \to \infty$, i.e., when the interface is solid. The dots are the values of the protrusion heights calculated using the analytical formulas by Schönecker *et al.* [27] for a flat interface, and excellent agreement is found with our results in that limit.

protrusion heights, which can be found on the basis of the theory by Schönecker *et al.* [27] for the case of a flat interface ($\Phi = 1$). The agreement is excellent, for both $h_\parallel$ and $h_\perp$, providing another validation of the numerics described here. Our results further demonstrate that the behavior of the

slip lengths with Φ is not trivial when the viscosity ratio varies, as the figure well exemplifies. In particular, as soon as $\lambda > 1$, the protrusion height $h_\perp$ presents a maximum for a value of Φ slightly larger than unity. The maximum position is, however, not constant and moves slightly leftward as λ increases. This slip length keeps reducing with the increase of the viscosity ratio until $\lambda = 1$ is reached. A further increment of λ profoundly changes the trend of $h_\perp$, which, from this point on, will no longer present a maximum. We can note that for values of λ approximately greater than 5, the curve becomes very close to the dashed line reported in Fig. 5, which corresponds to the slip length computed with the no-slip condition applied over the interface. This result is consistent with the fact that a lubricant fluid with a large viscosity compared to that of the working flow, in practice, behaves like a solid wall, minimizing the slippage and drastically reducing the drag reduction performance of the surface. Finally, we note that the protrusion height shows an asymmetric behavior with respect to the unitary value of Φ (i.e., flat interface). For a given value of c, increasing the volume fraction after the optimal value, the slip length starts to monotonically decrease following a quasilinear variation, whose slope is almost independent of the viscosity ratio. Reducing the volume fraction, we obtain that the value of the slip length $h_\perp$ decreases again but never crosses the limit delineated by the dashed line since, in the limit of $\Phi \to 0$, the geometry behaves like riblets, similar to those studied by Luchini *et al.* [43] and by García-Mayoral and Jiménez [50].

For the parallel protrusion heights $h_{||}$, reported in the right column of Fig. 5, we can extract similar features to those discussed for $h_\perp$. Again there is a strong dependency on the viscosity ratio, and the magnitude of the parallel protrusion height increases as λ decreases. The reduction of the slip length $h_\parallel$ is not linear with the increase of the viscosity ratio. The fact that the reduction of the protrusion height does not scale linearly with the reduction of the viscosity ratio is potentially a favorable behavior which hypothetically permits us to use a couple of fluids forming a more robust interface, while minimizing the penalty associated with the increase of the viscosity ratio. The longitudinal slip lengths do not exhibit a maximum as function of the volume fraction, but keep increasing with Φ, for $\lambda < 1$, while showing an opposite and nonsymmetric trend with respect to the value of the viscosity ratio. This particular behavior of the parallel slip length was also reported by Ng and Wang [24], who allowed a partial slip over the interface by means of the Navier boundary condition with an intrinsic slip length. Also in this case, for a large value of λ the curves collapse on the dashed line, representing the longitudinal protrusion height for the no-slip condition applied on the interface. Thus, it is found again that a large viscosity of the lubricant fluid leads the interface to behave similarly to a no-slip wall.

It is now important to underline, that the stand-alone values of the protrusion heights may have a small relevance when a turbulent flow over an SHS or LIS is being considered. As pointed out by Luchini [51], the parameter that controls the drag reduction to leading order is the difference between the slip lengths: the larger is this difference, the larger will be the drag reduction to be expected. This topic is discussed in the next section. Following this criterion, it is useful to look at this difference reported in Fig. 6. The best drag reduction, at any given viscosity ratio, is expected for the most protruding bubble, while the worst scenario coincides with the value of Φ which maximizes the transverse protrusion height, corresponding to an inflection of the curves representing $\Delta h = h_{||} - h_\perp$. These considerations are expected not to be valid if the typical size of the bubble mattress becomes comparable to the size of the viscous sublayer. In this case, especially for the LIS cases involving a high viscosity ratio, a surface roughness behavior is expected [52], turning the drag reduction into a drag increase.

The flow field for both longitudinal and transverse flow can be reconstructed within the microscopic domain and is shown in Fig. 7 for a representative case at $\lambda = 20$, $c = 0.50$, $\mathrm{Ca} = 0.10$, for two values of Φ. As expected, it consists in a recirculation zone taking place between the wall cavity and the interface for the transverse flow, while a linear velocity profile is established for both u and w at a sufficient distance above the interface.

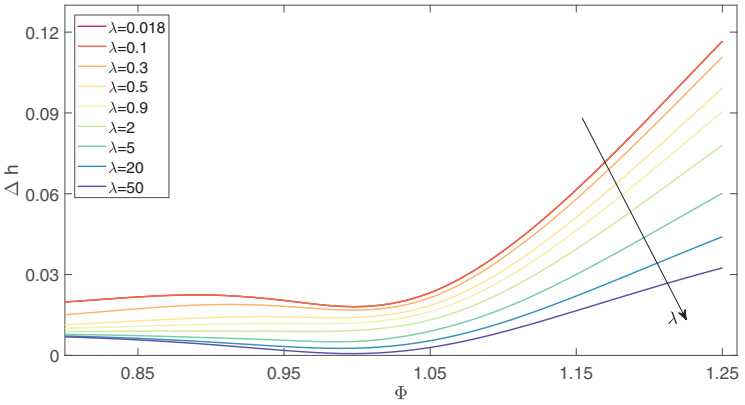

(a)

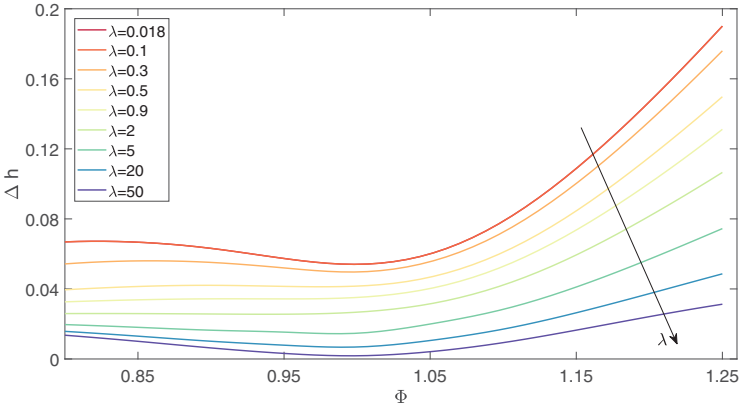

(b)

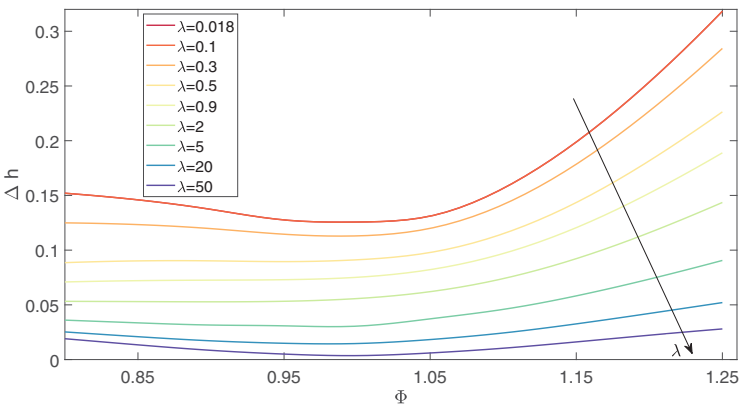

(c)

FIG. 6. Computed difference between transverse and longitudinal protrusion heights for increasing values of c and a wide range of λ at Ca $= 0.1$. The value of the interface span c is increased from top to bottom, from $c = 0.30$ to $c = 0.70$.

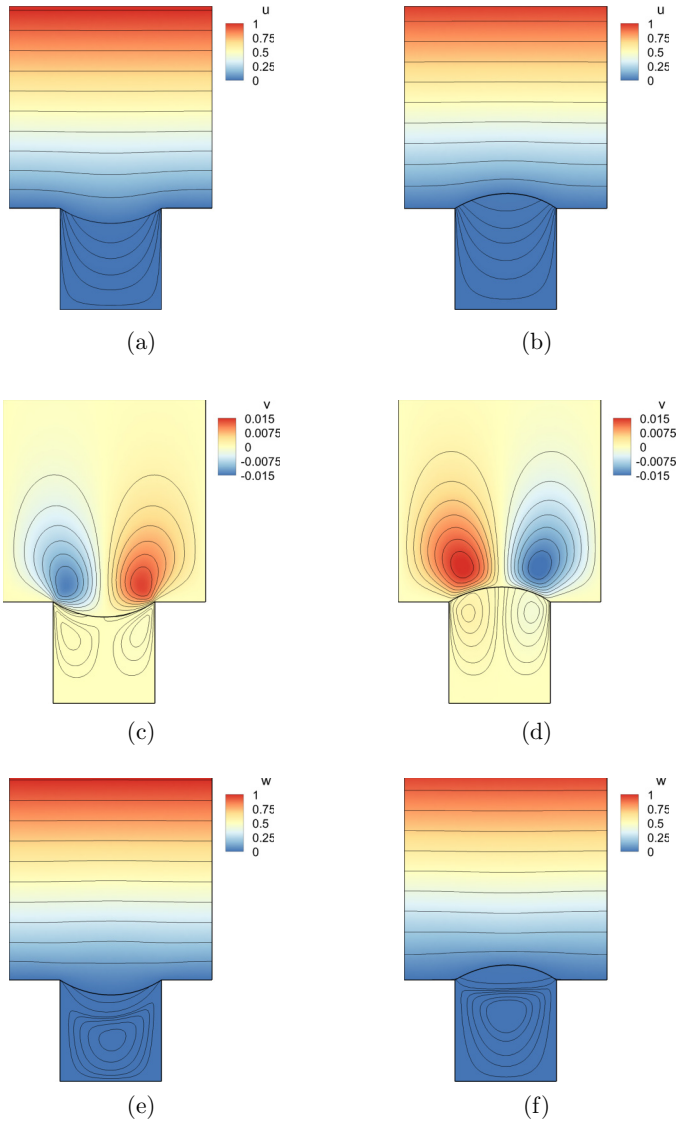

FIG. 7. Flow field developing into the computational domain for two representative cases with a depressing (left, $\Phi = 0.90$) and protruding (right, $\Phi = 1.10$) interface at $\lambda = 20$ and $\mathrm{Ca} = 0.1$. (a), (b) longitudinal velocity component; (c), (d) wall normal velocity component; (e), (f) transverse velocity component.

III. LIMITATIONS OF THE NAVIER SLIP CONDITION

In this section, we briefly discuss how the results obtained in the previous section can be used to estimate the drag reduction induced by SHS or LIS coatings in a turbulent flow. The key idea is to use the calculated values of the protrusion heights to model the slippage at each wall by means of an equivalent boundary condition applied at a fictitious and smooth surface. The standard setup involves the simulation of a turbulent channel flow, such as that described in Kim *et al.* [53], but changing the wall boundary conditions according to (1). The described setup has already been studied, first by Min and Kim [32], and more extensively by Busse and Sandham [36]; thus, in the present paper, we aim to highlight only some aspects related to the range of applicability of the protrusion height approach and make some considerations on the drag reduction.

The reason behind the drag reduction is to be found close to the wall and in the effect that a slip velocity has on the near-wall turbulence. On the one hand, an increase of slip in the streamwise direction (i.e. a large value of the longitudinal slip length) tends to reduce skin friction and attenuate the wall cycle. On the other hand, a spanwise slip has a much less trivial effect. As shown by Choi *et al.* [54] and Min and Kim [32], the creation of a slip velocity in the spanwise direction tends to increase the drag because of the enhancement of the strength of the near-wall streamwise vortices. The skin-friction drag reduction for a combined longitudinal and transverse slip is a consequence of the competition between these two mechanisms. Following the theory developed by Luchini *et al.* [43], the most important length scale governing the skin-friction drag is the difference between the protrusion heights, for anisotropic small surface protrusions embedded within the viscous sublayer. However, this is not always the case since some drag reduction is indeed observed, as demonstrated by Busse and Sandham [36] [see Fig. 8(a)], also when $\Delta h = 0$. This is consistent with the observation of drag reduction in isotropic lattices (e.g., circular posts), where the slip lengths are equal. The error committed in considering the drag reduction as a function only of the difference between the protrusion heights increases with the increase of the value of the longitudinal slip.

It is useful to stress the fact that not all the zones in the plot of Fig. 8(a) are of practical and physical relevance, since the Navier boundary condition is demonstrated to be valid only up to a certain level of slip. To fix our ideas, let us look in more detail at the simulations conducted by Luchini [40]. He considered the wall coated by longitudinal no-shear stripes, mimicking a superhydrophobic surface with a flat interface between the phases. The ratio between the interface span and the texture periodicity b was fixed to 0.5, and a series of direct numerical simulations at $\mathrm{Re}_\tau \approx 180$ were conducted for different values of b. He demonstrated that the protrusion heights yield very similar results to those obtained by taking into account the real wall texture up to $b^+ \approx 20$. The protrusion heights normalized by the periodicity for such walls are easily calculated from Philip's theory and are $h_{||} = 0.110$ and $h_\perp = 0.055$, respectively. Considering the upper bound of $b^+ = 20$, it is easy to find that, in wall units, the slip lengths are $h_{||}^{+0} \approx 2.2$ and $h_\perp^{+0} \approx 1.1$, where the superscript "0+" means that the protrusion heights are expressed in wall units based on the nominal Re_τ. Inside this region a particular trend of the drag reduction can be identified and demonstrated. It has been proposed by Luchini [51] that

$$\frac{C_f}{C_{f_0}} = 1 - \frac{\Delta h^+}{(2C_{f_0})^{-\frac{1}{2}} + (2k)^{-1}}, \tag{27}$$

where C_{f_0} is the reference friction factor for the standard no-slip wall at the actual Re_τ and k is von Kármán's constant, which we can take equal to 0.41.

We refer only to the drag reducing region since, for the particular wall texture under investigation in this work, $h_{||} > h_\perp$, and the only possible effect is a drag reduction. Figure 8(b) shows a comparison between the analytical formula (27) and the numerical simulations results obtained by collecting data from Min and Kim [32], Busse and Sandham [36], and our numerical simulations, using some of the values of protrusion heights computed in the previous section. The values of Δh are normalized using the actual friction velocity ($u_\tau = \sqrt{\tau_w/\rho} = u_{\tau_0}\sqrt{\frac{C_f}{C_{f_0}}}$) as the velocity scale, which is a more suitable choice with respect to u_{τ_0}, since Re_τ changes with wall slippage. The correlation between the numerical data and the linear relation (27) turns out to be very satisfactory in the region bounded by the dashed lines in Fig. 8(a), where the maximum values of the protrusion heights are $h_{||}^{+0} \approx 3.0$ and $h_\perp^{+0} \approx 1.5$.

What we can conclude from the above reasoning is that the protrusion heights approach has a rather narrow region of validity, but in this region the drag reduction is well correlated with Δh^+ via the formula (27). If the values of the protrusion heights are too large, then the drag reduction cannot be predicted by Δh^+, but, in this case, the Navier boundary condition itself is no more a reliable model of the real wall configuration.

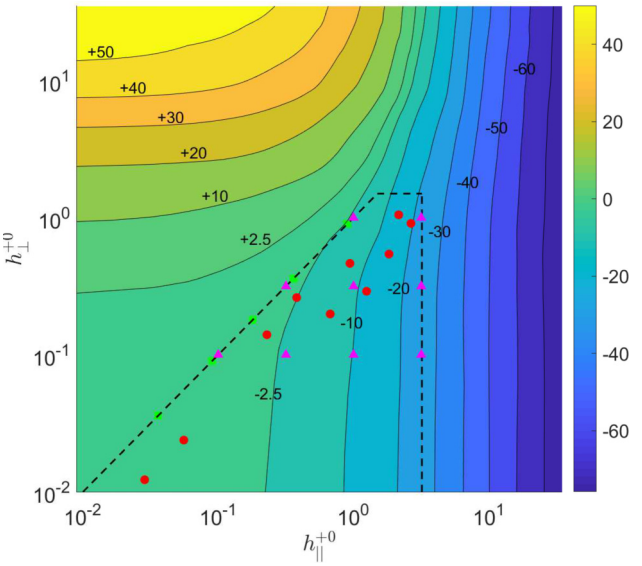

(a)

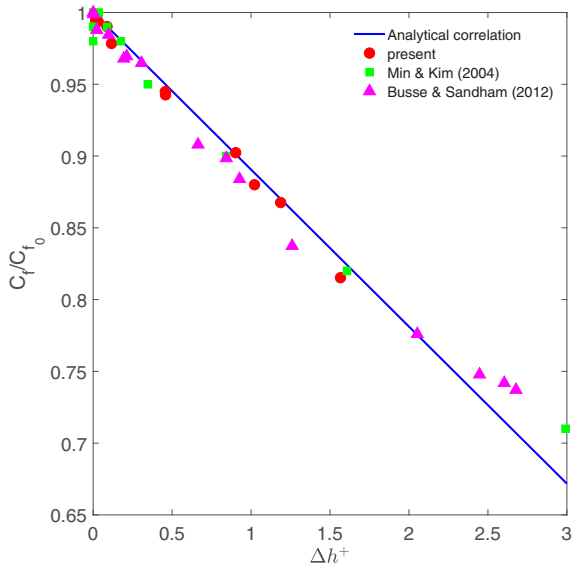

(b)

FIG. 8. (a) Estimated limits of validity of relation (27) (region enclosed by dashed lines) together with the present simulations (red circles), those by Min and Kim [32] (green squares), and those by Busse and Sandham [36] (magenta triangles). The isocontours with labels show the percentage drag increase or reduction at $\mathrm{Re}_\tau = 180$ as computed by Busse and Sandham [36]. (b) Friction factors as function of the difference in protrusion heights in wall units.

IV. CONCLUSIONS

The flow over superhydrophobic and liquid-impregnated surfaces has been studied from two points of view: the microscopic and the macroscopic one. The microscopic problem has attempted to remove some approximations used in previous models simulating the flow in the proximity of wall

asperities filled with gas or oil, taking into account different viscosity ratios between the working and the lubricant fluid and the effect of surface tension. The main goal of this problem was the derivation of the protrusion heights as function of the salient geometrical and physical parameters of the problem, since they are a direct measure of the drag reduction properties of such coatings. The macroscopic problem has involved direct numerical simulations of a turbulent flow in a plane channel at moderate Reynolds number; the slippage at the walls has been modeled through the Navier boundary conditions, which directly employ the values of the protrusion heights coming from the solution of the microscopic problem. The achievements and conclusions of this work can be summarized as follows:

A boundary integral formulation for the longitudinal and the transverse flow above SHS or LIS longitudinal grooves has been proposed, and the numerical results obtained by the boundary element method have been extensively validated.

The viscosity ratio λ between the fluids in contact has shown a major nontrivial effect in the variation of both protrusion heights. The present results confirm the trend delineated by Schönecker *et al.* [27] and extend them to the general case of nonflat interfaces.

We have identified the region of applicability of the protrusion heights approach [formula (27)] for a specific roughness pattern: $(h_{||}^{+0}, h_{\perp}^{+0}) \in [0, 3] \times [0, 1.5]$. In this portion of space, Δh can be conveniently considered as the key indicator of the drag reducing properties of the surface. This is no more the case for high absolute values of the protrusion heights, as pointed out by Luchini [40] and Seo and Mani [41]; in this case the use of the homogenized condition by Navier is questionable, and a more sophisticated wall treatments is needed, accounting for the interactions between the near-wall fluctuating field and the outer flow.

The first works which fully account for the inner-outer interaction are starting to appear (see, for example, Cartagena *et al.* [42]). This approach works well if the surface provides a relatively large level of slip, but it is tremendously expensive and numerically very challenging because of the interface deformation over very short timescales. Since in practice both SHSs and LISs are sensitive to lubricant layer depletion, a homogenized approach such as the one employed here, possibly with time-varying slip lengths, remains an attractive alternative.

ACKNOWLEDGMENTS

Our activities on SH and LIS coatings have started thanks to a gratefully acknowledged Fincantieri Innovation Challenge grant, monitored by Cetena S.p.A. (with Giovanni Caprino as program officer). We thank Ricardo García-Mayoral for interesting discussions and for providing the data to trace isocontours in Fig. 8(a).

[1] M. J. Walsh, Effect of detailed surface geometry on riblet drag reduction performance, J. Aircr. **27**, 572 (1990).

[2] W. Barthlott and C. Neinhuis, Purity of the sacred lotus, or escape from contamination in biological surfaces, Planta **202**, 1 (1997).

[3] H. A. Stone, A. D. Stroock, and A. Ajdari, Engineering flows in small devices: Microfluidics toward a lab-on-a-chip, Annu. Rev. Fluid Mech. **36**, 381 (2004).

[4] J. Ou, B. Perot, and J. P. Rothstein, Laminar drag reduction in microchannels using ultrahydrophobic surfaces, Phys. Fluids **16**, 4635 (2004).

[5] J. Ou and J. P. Rothstein, Direct velocity measurements of the flow past drag-reducing ultrahydrophobic surfaces, Phys. Fluids **17**, 103606 (2005).

[6] C.-H. Choi and C.-J. Kim, Large Slip of Aqueous Liquid Flow Over a Nanoengineered Superhydrophobic Surface, Phys. Rev. Lett. **96**, 066001 (2006).

[7] J. Ou and J. P. Rothstein, Drag reduction in turbulent flows over superhydrophobic surfaces, Phys. Fluids **21**, 085103 (2009).
[8] D. Byun, J. Kim, H. S. Ko, and H. C. Park, Direct measurement of slip flows in superhydrophobic microchannels with transverse grooves, Phys. Fluids **20**, 113601 (2008).
[9] E. Karatay, A. S. Haase, C. W. Visser, C. Sun, D. Lohse, P. A. Tsai, and R. G. H. Lammertink, Control of slippage with tunable bubble mattresses, Proc. Natl. Acad. Sci. USA **110**, 8422 (2013).
[10] G. Bolognesi, C. Cottin-Bizonne, and C. Pirat, Evidence of slippage breakdown for a superhydrophobic microchannel, Phys. Fluids **26**, 082004 (2014).
[11] J. S. Wexler, I. Jacobi, and H. A. Stone, Shear-Driven Failure of Liquid-Infused Surfaces, Phys. Rev. Lett. **114**, 168301 (2015).
[12] A. K. Epstein, T.-S. Wong, R. A. Belisle, E. M. Boggs, and J. Aizenberg, Liquid-infused structured surfaces with exceptional anti-biofouling performance, Proc. Natl. Acad. Sci. USA **109**, 13182 (2012).
[13] S. Ozbay, C. Yucee, and H. Y. Erbil, Improved icephobic properties on surfaces with a hydrophilic lubricating liquid, ACS Appl. Mater. Interfaces **39**, 22067 (2015).
[14] B. R. Solomon, K. S. Khalil, and K. K. Varanasi, Drag reduction using lubricant-impregnated surfaces in viscous laminar flow, Langmuir **30**, 10970 (2014).
[15] B. J. Rosenberg, T. Van Buren, M. K. Fu, and A. J Smits, Turbulent drag reduction over air- and liquid-impregnated surfaces, Phys. Fluids **28**, 015103 (2016).
[16] C. L. M. H. Navier, Mémoire sur les lois du mouvement des fluides, Mem. Acad. R. Sci. Inst. Fr. **6**, 389 (1823).
[17] J. R. Philip, Flows satisfying mixed no-slip and no-shear conditions, Z. Angew. Math. Phys. **23**, 353 (1972).
[18] E. Lauga and H. A. Stone, Effective slip in pressure-driven Stokes flow, J. Fluid Mech. **489**, 55 (2003).
[19] A. M. J. Davis and E. Lauga, Geometric transition in friction for flow over a bubble mattress, Phys. Fluids **21**, 011701 (2009).
[20] D. Crowdy, Slip length for longitudinal shear flow over a dilute periodic mattress of protruding bubbles, Phys. Fluids **22**, 121703 (2010).
[21] J. Hyväluoma and J. Harting, Slip Flow Over Structured Surfaces with Entrapped Microbubbles, Phys. Rev. Lett. **100**, 246001 (2008).
[22] M. Sbragaglia and A. Prosperetti, Effective velocity boundary condition at a mixed slip surface, J. Fluid Mech. **578**, 435 (2007).
[23] C. J. Teo and B. C. Khoo, Flow past superhydrophobic surfaces containing longitudinal grooves: Effects of interface curvature, Microfluid. Nanofluid. **9**, 499 (2010).
[24] C.-O. Ng and C. Y. Wang, Effective slip for stokes flow over a surface patterned with two- or three-dimensional protrusions, Fluid Dyn. Res. **43**, 065504 (2011).
[25] D. Crowdy, Effective slip lengths for longitudinal shear flow over partial-slip circular bubble mattresses, Fluid Dyn. Res. **47**, 065507 (2015).
[26] D. Crowdy, Slip length for transverse shear flow over a periodic array of weakly curved menisci, Phys. Fluids **29**, 091702 (2017).
[27] C. Schönecker, T. Baier, and S. Hardt, Influence of the enclosed fluid on the flow over a microstructured surface in the Cassie state, J. Fluid Mech. **740**, 168 (2014).
[28] A. V. Belyaev and O. I. Vinogradova, Effective slip in pressure-driven flow past super-hydrophobic stripes, J. Fluid Mech. **652**, 489 (2010).
[29] A. I. Ageev and N. A. Osiptsov, Stokes flow over a cavity on a superhydrophobic surface containing a gas bubble, Fluid Dyn. **50**, 748 (2015).
[30] A. I Ageev, I. V. Golubkina, and A. N. Osiptsov, Application of boundary element method to Stokes flows over a striped superhydrophobic surface with trapped gas bubbles, Phys. Fluids **30**, 012102 (2018).
[31] Y. Li, K. Alame, and K. Mahesh, Feature-resolved computational and analytical study of laminar drag reduction by superhydrophobic surfaces, Phys. Rev. Fluids **2**, 054002 (2017).
[32] T. Min and J. Kim, Effects of hydrophobic surface on skin-friction drag, Phys. Fluids **16**, L55 (2004).
[33] K. Fukagata and N. Kasagi, A theoretical prediction of friction drag reduction in turbulent flow by superhydrophobic surfaces, Phys. Fluids **18**, 051703 (2006).

[34] M. B. Martell, J. B. Perot, and J. P. Rothstein, Direct numerical simulations of turbulent flows over superhydrophobic surfaces, J. Fluid Mech. **620**, 31 (2009).
[35] M. B. Martell, J. P. Rothstein, and J. B. Perot, An analysis of superhydrophobic turbulent drag reduction mechanisms using direct numerical simulation, Phys. Fluids **22**, 065102 (2010).
[36] A. Busse and N. D. Sandham, Influence of an anisotropic slip-length boundary condition on turbulent channel flow, Phys. Fluids **24**, 055111 (2012).
[37] S. Turk, G. Daschiel, A. Stroh, Y. Hasegawa, and B. Frohnapfel, Turbulent flow over superhydrophobic surfaces with streamwise grooves, J. Fluid Mech. **747**, 186 (2014).
[38] J. Seo, R. García-Mayoral, and A. Mani, Pressure fluctuations and interfacial robustness in turbulent flows over superhydrophobic surfaces, J. Fluid Mech. **783**, 448 (2015).
[39] J. Seo, R. García-Mayoral, and A. Mani, Turbulent flows over superhydrophobic surfaces: Flow-induced capillary waves, and robustness of air-water interfaces, J. Fluid Mech. **835**, 45 (2018).
[40] P. Luchini, The relevance of longitudinal and transverse protrusion heights for drag reduction by a superhydrophobic surface, in *Proc. European Drag Reduction and Flow Control Meeting—EDRFMC 2015; March 23–26, 2015*, edited by K.-S. Choi and R. García-Mayoral (Cambridge, UK, 2015), pp. 81–82.
[41] J. Seo and A. Mani, On the scaling of the slip velocity in turbulent flows over superhydrophobic surfaces, Phys. Fluids **28**, 025110 (2016).
[42] E. J. G. Cartagena, I. Arenas, M. Bernardini, and S. Leonardi, Dependence of the drag over super hydrophobic and liquid infused surfaces on the textured surface and Weber number, Flow Turbul. Combust. **100**, 945 (2018).
[43] P. Luchini, F. Manzo, and A. Pozzi, Resistance of a grooved surface to parallel flow and cross-flow, J. Fluid Mech. **228**, 87 (1991).
[44] C. Cottin-Bizonne, B. Cross, A. Steinberger, and E. Charlaix, Boundary Slip on Smooth Hydrophobic Surfaces: Intrinsic Effects and Possible Artifacts, Phys. Rev. Lett. **94**, 056102 (2005).
[45] E. Alinovi and A. Bottaro, A boundary element method for Stokes flows with interfaces, J. Comput. Phys. **356**, 261 (2018).
[46] C. Pozrikidis, *A Practical Guide to Boundary Element Methods with the Software Library BEMLIB* (CRC Press, Boca Raton, FL, 2002).
[47] A. Steinberger, C. Cottin-Bizonne, P. Kleimann, and E. Charlaix, High friction on a bubble mattress, Nat. Mater. **6**, 665 (2007).
[48] P. Than, L. Preziosi, D. D. Josephl, and M. Arney, Measurement of interfacial tension between immiscible liquids with the spinning road tensiometer, J. Colloid Interface Sci. **124**, 552 (1988).
[49] C. Roelands, Correlational aspects of the viscosity-temperature-pressure relationship of lubricating oils, Ph.D. thesis, TU Delft (1966).
[50] R. García-Mayoral and J. Jiménez, Drag reduction by riblets, Phil. Trans. Royal Soc. London A **369**, 1412 (2011).
[51] P. Luchini, Reducing the turbulent skin friction, in *Computational Methods in Applied Sciences '96*, edited by J.-A. Désidéri *et al.* (John Wiley & Sons, Chichester, 1996), pp. 466–470.
[52] J. Jiménez, Turbulent flows over rough walls, Annu. Rev. Fluid Mech. **36**, 173 (2004).
[53] J. Kim, P. Moin, and R. Moser, Turbulence statistics in fully developed channel flow at low Reynolds number, J. Fluid Mech. **177**, 133 (1987).
[54] H. Choi, P. Moin, and J. Kim, Active turbulence control for drag reduction in wall-bounded flows, J. Fluid Mech. **262**, 75 (1994).